



Finite element study of multi-modal vibration damping for thermal barrier coating applications

F. Casadei ^{*}, K. Bertoldi, D.R. Clarke

School of Engineering and Applied Sciences, Harvard University, Cambridge, MA, United States



ARTICLE INFO

Article history:

Received 3 May 2013

Received in revised form 1 July 2013

Accepted 18 July 2013

Available online 19 August 2013

Keywords:

Vibration damping

Thermal barrier coating

Anelastic relaxation

Finite element modeling

ABSTRACT

A physically-based computational model is developed to predict the damping behavior of oxide thermal barrier coating systems. The constitutive damping model is derived from the theory of point defect relaxation in crystalline solids and implemented within a finite element framework. While oxide coatings have been primarily employed as thermal barriers for gas turbine blades, there is a growing interest in developing multifunctional coatings combining thermal protection and damping capabilities. The direct frequency response method, as well as the modal strain energy method, have been implemented to evaluate the functional dependence of damping on temperature and frequency. Numerical results are validated through the limited experimental data available in the literature, and new results are presented to illustrate the effects of different topcoat oxides. The paper also illustrates how the developed methodology enables the damping capacity under different vibrational modes to be predicted, and to estimate the sensitivity of the design for varying geometrical parameters. Finally, the computational model is applied to investigate the damping performance of an oxide-coated turbine blade.

© 2013 Elsevier B.V. All rights reserved.

1. Introduction

Developing vibration damping methods is critical in many technologies and especially so for gas turbine engines since many of their rotating components have to operate under a combination of highly exacting temperature creep-fatigue conditions and with high dimensional tolerances [1]. For instance, in the compressor and hot sections of the turbine, the blades have to withstand both high inertial stresses and repeated buffeting as they continuously rotate past stationary blades being periodically shadowed. Depending on the details of the design, these buffeting frequencies are in the 10 kHz range. Currently, damping is introduced by using mechanical dampers included under each blade, as well as through damped supports [2]. Dangerous resonances are avoided by deliberately mistuning the resonant frequencies of individual blades on a disk [3], and by controlling the spinning up of the turbine to avoid resonances.

One of the advances made in gas turbine technologies, has been the widespread use of thermal barrier coatings applied to the surface of blades to provide thermal protection to the superalloy components. These coatings have enabled the turbine operating temperatures to be increased, facilitating improved energy

efficiency, while minimizing increased metal temperatures [4–7]. While their primary function is as a refractory, there is also interest in developing coatings with dual functionality, combining thermal protection and damping capabilities [8–11].

In evaluating a new damping material for use in an application such as a coating, the design engineer is faced with a number of challenges. One is to predict the behavior of a material under a variety of conditions based only on a limited amount of data. Another is to establish the behavior of a complex shaped component, such as an airfoil blade, that consists of an alloy and a coating whose properties are different at different temperatures. As we will show in this contribution, a physically-based computational model can be used to address these questions.

The organization of this paper is as follows. First, we present data on the damping behavior of materials used in current thermal barrier coatings and superalloy as well as some other candidate oxides. This data will be used as input for the damping computations. Then, we briefly describe the point defect rearrangement mechanism which is used as a basis for the constitutive model of damping. The model is then implemented in a finite element analysis using both the direct frequency response method and the modal strain energy method. The numerical results are compared to the experimental data presented in Section 2, for the purpose of validating them. Then, the damping of a simple cantilever beam under different vibrational modes is calculated.

^{*} Corresponding author. Address: Harvard University, 29 Oxford Street, Cambridge, MA, United States. Tel./fax: +1 4044147912.

E-mail address: fcasadei@seas.harvard.edu (F. Casadei).

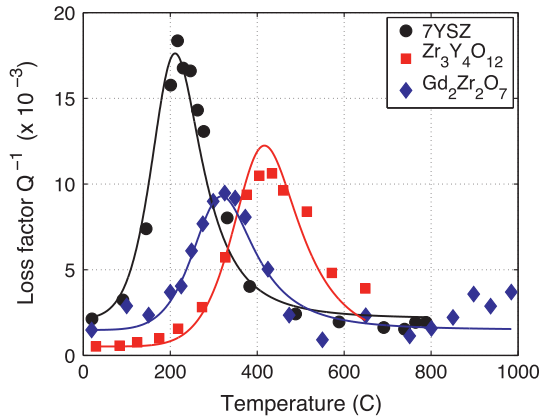


Fig. 1. Comparison between the temperature dependent flexural damping of three oxides in the kHz frequency range. The curves through the data represent the best fit to the constitutive model described in Section 3.

Finally, the computational method is used to investigate the damping capacity of a turbine blade shaped specimen.

2. Damping in thermal barrier coating systems

Thermal barrier coatings (TBCs), currently in use, typically consist of 7 weight% yttria-stabilized zirconia (7YSZ) deposited on a superalloy with a thin, intermediate alloy interlayer.¹ Other oxide compositions, including $\text{Gd}_2\text{Zr}_2\text{O}_7$ and $\text{Zr}_3\text{Y}_4\text{O}_{12}$, have also been investigated as alternative TBCs [12]. The superalloys of interest are primarily second-generation nickel-based alloys, such as the commercial PWA 1484, CMSX-4 and N5 single crystal alloys [13].

The damping characteristics of all these materials have been measured for flexural beam configurations by means of the frequency response method [14,15]. Measurements are conducted under small displacement conditions from room temperature up to a maximum of about 1000 °C. The functional dependence of damping on temperature for the three oxides mentioned above is shown in Fig. 1. Although in all these materials damping is believed to originate from similar defect mechanisms [15], their damping peaks occur at significantly different, albeit moderate, temperatures, between 200 °C and 500 °C.

A second experiment is performed to compare the loss factor of a PWA 1484 superalloy beam with and without a 142 μm thick 7YSZ coating. Fig. 2 illustrates that the 7YSZ coating produces a damping peak at a temperature of about 200 °C that is absent in the bare superalloy. This observation is similar to the one obtained from internal friction measurements of single crystal zirconia in [16], and is consistent with the experimental results obtained for dense 7YSZ in Fig. 1. Moreover, consistently with results presented in [14], Fig. 2 shows a clearly defined damping peak at temperatures above 900 °C that has been attributed to Ni and Al diffusional hopping in the γ' phase [17].

While such observations can give some guidance as to other possible compounds may also exhibit damping, they provide little knowledge on how such property carries over to other vibration modes, or what are the effects of different geometrical parameters of TBC assemblies. To address these questions, this paper proposes a physically-based computational tool which incorporates a constitutive model of damping based on point defect rearrangement. This mechanism is briefly described in the following section.

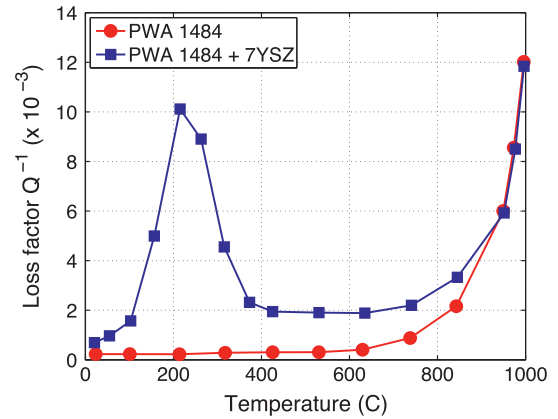


Fig. 2. Flexural vibration damping as a function of temperature for a thermal barrier coating system as well as data for the uncoated PWA-1484 superalloy.

3. Constitutive damping behavior

Point defect rearrangement under stress is the dominant mechanism of damping in dense defective oxides such as 7YSZ [18–20]. In many of these oxides, such as ThO_2 doped with CaO or ZrO_2 doped with Y_2O_3 , oxygen vacancies are created to charge compensate for the aliovalent dopant or stabilizer ion. The defect is typically a dipole consisting of an oxygen vacancy and the dopant ion, and it acts as both an electrostatic and an elastic dipole [21]. When the material is subject to an alternating stress at frequency ω , the individual point-defect dipoles can switch from one crystallographic orientation to another producing an anisotropic local distortion of the crystal lattice [22]. Mechanical damping resulting from this dipole switching mechanism was first analyzed by Wachtman [23] and the interested reader is referred to his and related analyses [22,24].

Briefly, the local distortion of a lattice containing point defects is described by a second-rank tensor λ characterizing the strain of the crystal with a unit concentration (mole fraction) of dipolar defects [22]. The dipole tensor can be expressed in terms of its principal values λ_i ($i = 1, 2, 3$) and a number n_t of independent orientations that depend on the defect's symmetry. The overall strain field is therefore given by the sum of two contributions:

$$\boldsymbol{\varepsilon} = \boldsymbol{\varepsilon}^{el} + \boldsymbol{\varepsilon}^{an} = \boldsymbol{\varepsilon}^{el} + \sum_{p=1}^{n_t} \lambda_p C_p \quad (1)$$

where $\boldsymbol{\varepsilon}^{el}$ is the elastic strain without defects, and $\boldsymbol{\varepsilon}^{an} = \sum_{p=1}^{n_t} \lambda_p C_p$ is an anelastic strain. In Eq. (1) λ_p denotes the dipole tensor for one of the n_t possible equivalent orientations of the defect, and $C_p = N_p/N_\mu$ is the mole fraction of defects in orientation p , where N_p and N_μ respectively denote the number of defects in orientation p , and the number of molecules per unit volume. If $n_t > 1$, defects characterized by different λ tensors interact differently with an applied stress field $\boldsymbol{\sigma}$ such that one is energetically favored over the others. This leads to a splitting of free-energy levels in which the probability of dipoles having different orientations is given by Boltzmann statistics [22,25]. The equilibrium values of C_p for the concentrations at any given stress and temperature (T) are therefore given by:

$$C_p = \frac{C_0 v_0}{n_t k_B T} \left[\lambda_p - \frac{1}{n_t} \sum_q \lambda_q \right] \boldsymbol{\sigma} \quad (2)$$

where C_0 is the total molar concentration of defects (constant), v_0 is the molecular volume, and k_B is the Boltzmann constant. To simplify the calculation here we consider only a homogeneous uniaxial state of stress (σ_{11}), the corresponding strain component (ε_{11}), as well as

¹ During use at high temperatures, a thin aluminum oxide layer (1–4 μm thick) forms under the 7YSZ coating.

λ tensor components λ_{11} . For the sake of clarity the subscript 11 will be omitted. Based on this assumption, the relaxation strength δ^* can be expressed as [26]:

$$\delta^* = \frac{\varepsilon^{an}}{\sigma} = \frac{C_0 v_0}{n_i k_B T} \left[\sum_p (\lambda_p)^2 - \frac{1}{n_t} \left(\sum_p \lambda_p \right)^2 \right] \quad (3)$$

The kinetics of defect rearrangement to a lower energy configuration is, in general, a time dependent process characterized by a relaxation time τ . The choice of using a single relaxation time is based on the experimental observations [23,26] that damping in simple oxides can occur by either cation interstitials (in rutile) or oxygen vacancies (in thoria), and give rise to a single damping peak. The presence of a relaxation time allows for the mechanical energy dissipated per unit cycle ΔU to be expressed through the following Debye function:

$$\Delta U = \delta^* \frac{\omega \tau}{1 + (\omega \tau)^2} \bar{\sigma}^2 \quad (4)$$

in which $\bar{\sigma}$ is the average applied stress. The defect relaxation is assumed to be a thermally activated process [23] described by the following Arrhenius equation:

$$\tau = \tau_0 \exp \left(\frac{\Delta E}{k_B T} \right) \quad (5)$$

where ΔE is the activation energy, and the pre-exponential factor τ_0 is a characteristic relaxation time related to the atomic jump rates inherent to specific defect mechanisms.

Substituting Eq. (5) into Eq. (4) yields

$$\Delta U = \delta^* \text{sech} \left(\ln \omega \tau_0 + \frac{\Delta E}{k_B T} \right) \bar{\sigma}^2 \quad (6)$$

which compared to the total vibrational energy $U = \bar{\sigma}^2 / 2Y$ allows expressing the internal friction or damping, Q^{-1} as:

$$Q^{-1} = \frac{\Delta U}{2\pi U} = \frac{YA}{k_B T} \text{sech} \left(\ln \omega \tau_0 + \frac{\Delta E}{k_B T} \right) \quad (7)$$

Here, Y denotes the Young's modulus, and A is a material parameter which is a function of the defects' concentration and orientation. Eq. (7) provides a direct constitutive relationship between macroscopic damping characteristics and atomic level mechanism. In the present work, this formulation is used to characterize the dissipation mechanism occurring in both the metallic superalloy and the oxide layers characterizing typical TBC systems.

4. Finite element analysis

Here, the constitutive damping behavior presented in the previous section is implemented within a linear FE framework. For this task, we adopt a phenomenological damping model based on the correspondence principle of linear viscoelasticity [27,28] whereby the inherent material dissipation is described in terms of a complex Young's modulus ($Y^* = Y' + iY''$ where $i = \sqrt{-1}$ is the imaginary unit) with the ratio of imaginary to real part being the material loss factor $Q^{-1} = Y''/Y'$. The choice of adopting a phenomenological model, compared, for example, to developing a statistical-mechanics based material law, is motivated by the need to accurately estimate the damping properties of complex systems with a modest computational effort. This is particularly relevant for the preliminary design of turbine blades in which several simulations are typically conducted to estimate the effects of a number of critical design parameters [29]. This section briefly describes both the direct frequency response method and the modal strain energy method that have been implemented as part of a in-house developed finite element (FE) code to predict the damping behavior of

complex TBC systems based on experimentally-informed material properties.

4.1. Direct frequency response method

The FE analysis of TBC systems with distributed dissipation mechanisms can be conveniently conducted in the frequency domain using the direct frequency response method [30]. If the structure undergoes harmonic motion at frequency ω , the generalized forces $\mathbf{f} \in \mathbb{R}^{n \times 1}$ and displacements $\mathbf{u} \in \mathbb{C}^{n \times 1}$ are related through the dynamic stiffness matrix of the structure as

$$[\mathbf{K}_1 + i\mathbf{K}_2(\omega, T) - \omega^2 \mathbf{M}] \mathbf{u} = \mathbf{f} \quad (8)$$

where $\mathbf{M} \in \mathbb{R}^{n \times n}$ and $\mathbf{K}_1 \in \mathbb{R}^{n \times n}$ are the global mass and stiffness matrices assembled using standard FE procedures [31], n denotes the global number of degrees of freedom. In the present notation, lower case bold letters denote vectors, while upper case bold letters are used for matrices. In Eq. (8) $\mathbf{K}_2(\omega, T) \in \mathbb{R}^{n \times n}$ is a hysteretic damping matrix which depends on the material loss factor (Q^{-1} in Eq. (7)) evaluated at frequency ω and temperature T . The hysteretic damping matrix of a system comprised of M different materials, each characterized by a loss factor Q_j^{-1} ($j = 1, 2, \dots, M$), is given by

$$\mathbf{K}_2(\omega, T) = \sum_{j=1}^M Q_j^{-1}(\omega, T) \mathbf{K}_1^{(j)} \quad (9)$$

in which

$$\mathbf{K}_1^{(j)} = \sum_{e=1}^{N_e^{(j)}} \mathbf{K}_1^e \quad (10)$$

is the portion of the global stiffness matrix assembled considering only the elemental contributions (\mathbf{K}_1^e) of the $N_e^{(j)}$ finite elements associated with the j th material property (see [31] for details).

The frequency response of the system is computed by solving Eq. (8) for the unknown nodal displacements $\mathbf{u}(\omega, T)$ within a frequency range of interest typically dictated by the spectral content of the externally applied loads. The vibration attenuation properties of the entire structure are then estimated in terms of a mechanical loss factor, or inverse quality (or gain) factor Q_{TBC}^{-1} defined as:

$$Q_{TBC}^{-1} = \frac{\Delta f}{f_r} \quad (11)$$

where Δf is the half power bandwidth (-3 dB) of the response at a resonance frequency f_r [32].

The major drawback of this approach is related to the need for assembling and factorizing a complex system of equations at each frequency step within the range of interest. For practical design purposes, the computational cost of direct frequency analyses may not be cost-effective especially when conducting several parametric analysis or optimization procedures.

4.2. Modal strain energy method

In order to reduce the computational costs associated with the direct frequency analysis, this research considers an alternative approach known as the modal strain energy method [30]. This approach avoids the direct solution of Eq. (8) by assuming that the damping coefficient of a structural mode is proportional to the loss factor of each material multiplied by the corresponding modal strain energy ratio (SER) [30]. If the structure is comprised of M different materials, the SER in the j th material layer is defined as

$$SER_j = \mathcal{U}_j / \mathcal{U}_{TOT} \quad (j = 1, 2, \dots, M) \quad (12)$$

where \mathcal{U}_j is the fraction of strain energy stored in the j th material, and

$$\mathcal{U}_{TOT} = \sum_{j=1}^M \mathcal{U}_j \quad (13)$$

is the total strain energy associated with an undamped vibrational mode of the system. Note that the r th undamped modal shape ϕ_r is obtained as the solution of the following real eigenvalue problem

$$[\mathbf{K}_1 - \omega_r^2 \mathbf{M}] \phi_r = 0 \quad (14)$$

from which the components of the strain energy in Eq. (12) are given by

$$\mathcal{U}_{TOT}^r = \frac{1}{2} \phi_r^T \mathbf{K}_1 \phi_r \quad \text{and} \quad \mathcal{U}_j^r = \frac{1}{2} \phi_r^T \mathbf{K}_1^{(j)} \phi_r \quad (15)$$

where $\mathbf{K}_1^{(j)}$ is defined in Eq. (10). Finally, the material loss factor associated with the r th mode of the structure is obtained as

$$(1/Q)^r = \sum_{j=1}^M \frac{\mathcal{U}_j^r}{\mathcal{U}_{TOT}^r} \times Q_j^{-1} = \sum_{j=1}^M \text{SER}_j \times Q_j^{-1} \quad (16)$$

This method is known to provide accurate predictions only for small values of damping, i.e. when $(1/Q)^r \ll 1.5$ [30]. Since for typical TBCs values of Q^{-1} range between 10^{-3} and 10^{-2} the modal strain energy method can be sufficiently accurate to give useful, though not necessarily exact, damping predictions.

5. Application to a coated beam system

5.1. Geometry and material properties

As an illustration, the numerical procedures presented in Section 4 are applied to predict the damping properties of a two-layer cantilever beam. The configuration, schematically shown in Fig. 3, corresponds to the one used in [14] to experimentally investigate the damping properties of a 7YSZ coated superalloy, and therefore allows to validate the FE predictions. The beam is $L = 16.9$ mm long, and is characterized by a rectangular cross section ($W = 5.03$ mm wide) comprised of a 0.38 mm thick PWA layer, and a 0.142 mm thick topcoat. In order to predict the effects of different topcoat materials on the damping properties of the TBC, analyses are conducted using the three oxides previously investigated (i.e. 7YSZ, $\text{Gd}_2\text{Zr}_2\text{O}_7$, and $\text{Y}_4\text{Zr}_3\text{O}_{12}$). The beam is rigidly clamped at its left end (cantilever) and is subjected to a concentrated point load $F(\omega)$ at the tip (Fig. 3). The geometry is discretized with a mesh comprising of 1920 linear (8-node) hexahedral elements, whose accuracy has been ascertained through a refinement study.

The activation energy (ΔE), relaxation time τ_0 , and relaxation strength (A) of the considered materials are summarized in Table 1. The constitutive damping parameters of the oxides are determined by fitting the experimental data presented in Fig. 1 through the functional dependance on frequency and temperature given by Eq. (7). The curves through the data in Fig. 1 represent the best fit to the adopted functional model. In order to extract the material

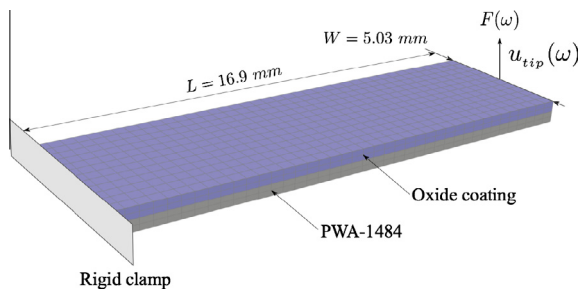


Fig. 3. Schematic of the two-material cantilever beam used in experiments.

Table 1

Anelastic relaxation parameters of the considered materials.

	ΔE (eV)	τ_0 (s)	A (-)
7YSZ	0.96	9.14×10^{-14}	6.51×10^{-14}
$\text{Gd}_2\text{Zr}_2\text{O}_7$	0.85	1.23×10^{-14}	4.51×10^{-14}
$\text{Y}_4\text{Zr}_3\text{O}_{12}$	1.01	8.21×10^{-15}	6.00×10^{-14}
PWA-1484	2.26	9.99×10^{-14}	1.09×10^{-14}

parameters for the PWA superalloy, the experimental data presented in [14] have been used. Additional data used in this work but not shown include the Young's modulus as a function of temperature for the superalloy and the 7YSZ coating [14,15]. The density of the PWA is assumed constant and equal to $\rho_{PWA} = 8700$ kg/m³, while an average density of $\rho_{TOP} = 4930$ kg/m³ is used for the oxide topcoats.

5.2. Numerical results

The vibration damping of the system is evaluated using both the modal strain energy method, and the direct frequency response method with frequency response functions evaluated in terms of the applied load $F(\omega)$ and the tip displacement u_{tip} (see Fig. 3).

5.2.1. 7YSZ coated beam

First the 7YSZ topcoat is considered and the computed results are compared with the experimental data provided in [14]. In order to investigate the functional dependance of damping on temperature, frequency response functions are computed for increasing temperatures from 0 to 900 °C (see Fig. 4). Interestingly, Fig. 4 illustrates how the FE model simultaneously captures the shift of the resonance peak induced by the Young's modulus reduction at higher temperatures, and the functional dependence of attenuation on temperature proper of the thermally activated relaxation mechanism considered herein.

The first four eigen modes of the beam, presented in Fig. 5, are also evaluated to estimate the modal damping using the strain energy method.

The evolution of the loss factor versus temperature is shown in Fig. 6 where numerical predictions are obtained both with the direct frequency response method, and the modal strain energy method. Remarkably, the results capture the damping peak temperature of about 200 °C induced by the 7YSZ phase, and are consistent with the general trend exhibited by the experimental data (available up to 900 °C). Some discrepancies in the amount of damping predicted by the FE model are observed especially at

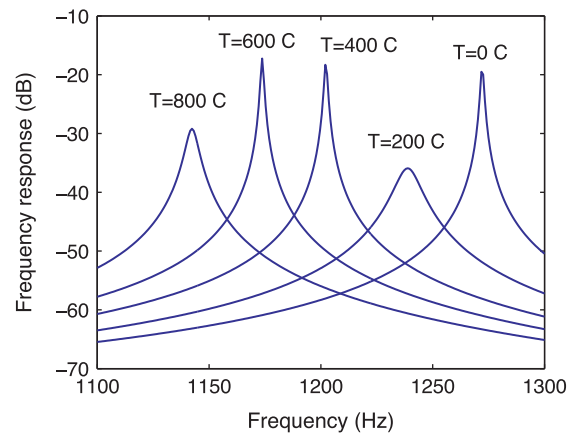


Fig. 4. Variation of the TBC's frequency response as a function of temperature. The shift of the resonance peak is induced by the reduction of the Young's modulus with increasing temperatures.

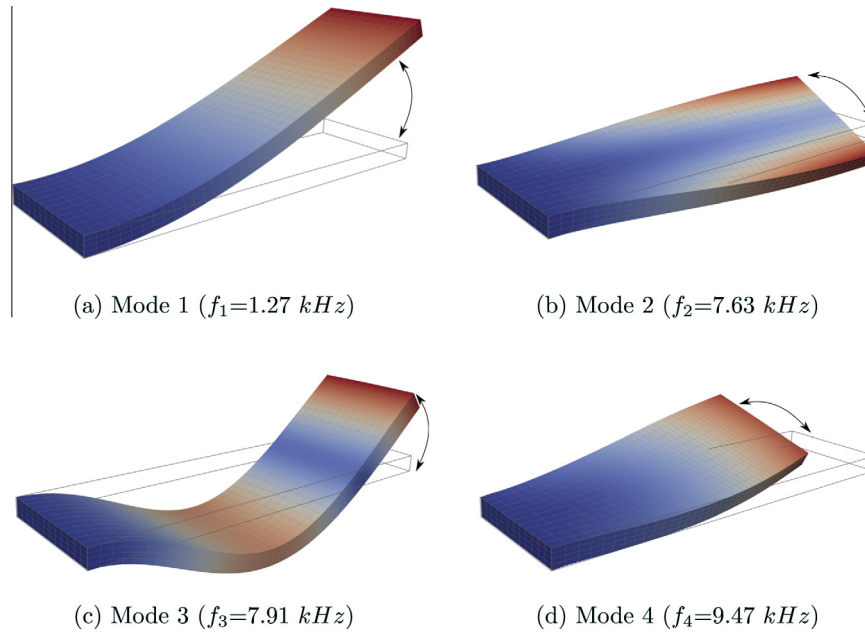


Fig. 5. First four normal modes of the undamped beam ($T = 0^\circ\text{C}$).

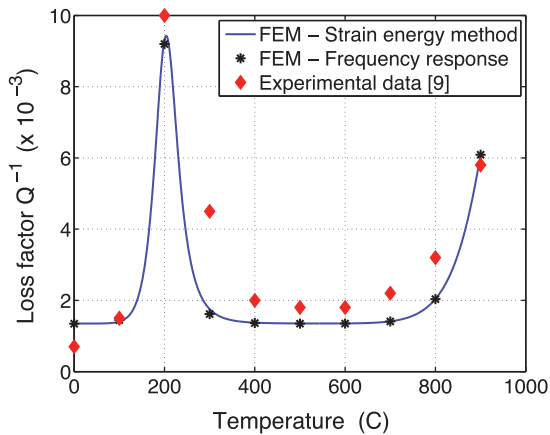


Fig. 6. Comparison between the numerical and experimental loss factor variations of the 7YSZ coated PWA superalloy beam.

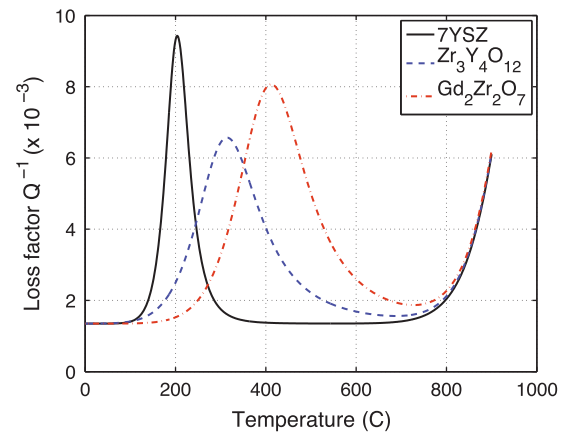


Fig. 7. Comparison between the loss factor variations of three TBCs featuring the same PWA-1484 superalloy and different topcoat oxides.

intermediate temperatures. This can be attributed to a temperature dependent background [33] generally not captured by the adopted model. Also consider that the contribution of the bond coat to the overall material loss of the TBC system has not been included due to insufficient experimental data available to calibrate the corresponding damping model. Fig. 6 also shows the excellent agreement between results computed with the direct frequency method and the strain energy approach. While the maximum discrepancy between the two sets of data is below 0.5% the modal strain energy method is found about 5 times faster than the direct frequency approach. For this reason the latter will be adopted in the following section to conduct sensitivity analyses for varying geometric parameters of the TBC.

5.2.2. Effect of different oxide coatings

A comparison between the damping of three TBCs featuring different coating oxides is shown in Fig. 7. Interestingly, the damping peak of each TBC occurs at the same peak temperature of the corresponding oxide phase, and it is in excellent agreement with the experimental data shown for the same oxides

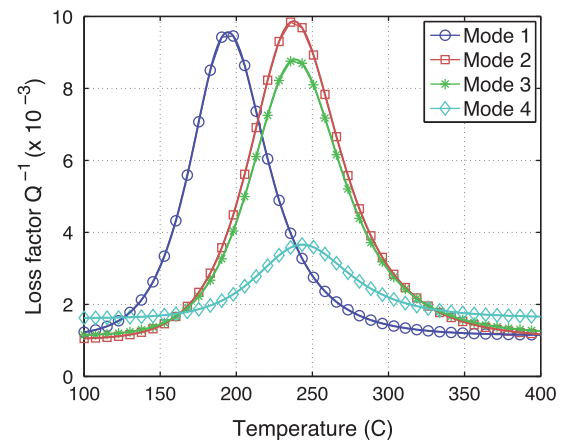


Fig. 8. Mechanical damping associated with different vibrational modes for the 7YSZ coated beam shown in Fig. 3.

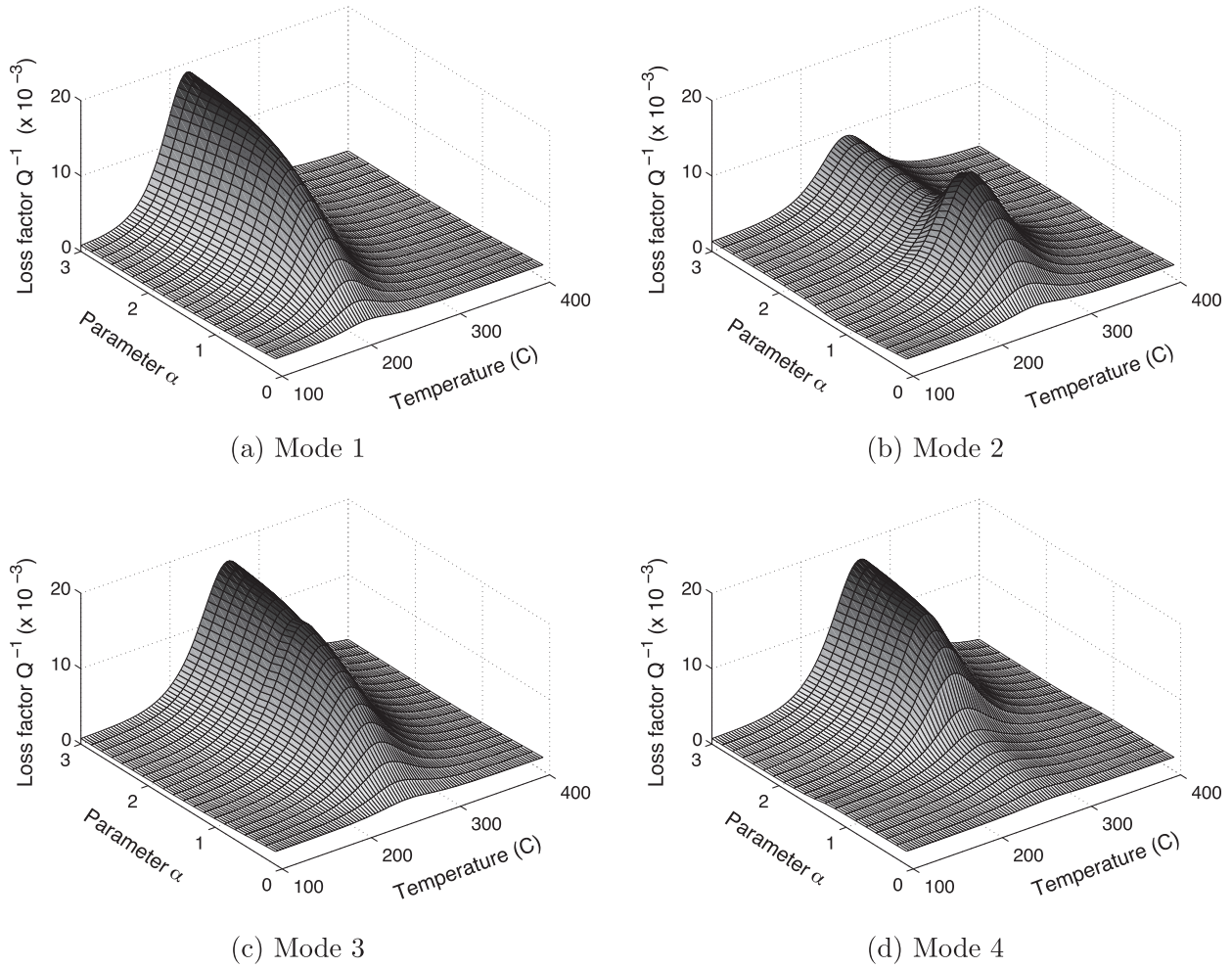


Fig. 9. Vibration damping associated to the first four eigenmodes of the TBC for different values of the 7YSZ layer thickness (t_{7YSZ}), and for $\beta = 1$.

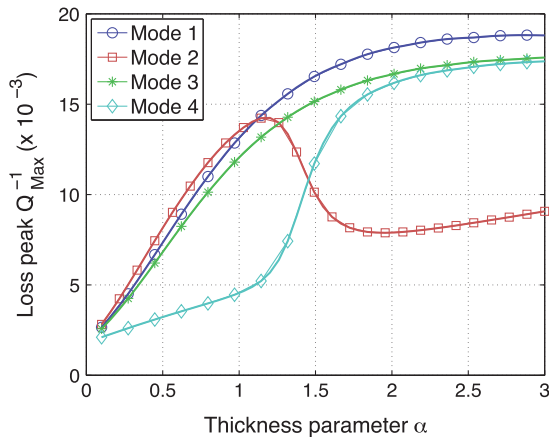


Fig. 10. Variation of the loss peak $Q_{Max}^{-1}(\alpha)$ associated to different vibration modes as a function of the thickness parameter α .

in Fig. 1. Whereas the peak temperature of the TBC is only dictated by the activation energy and relaxation time of its oxide layer, the maximum damping capacity of the system is also influenced by design features such as the thickness and width of each layer. The effects of such parameter on the damping performance of the TBC will be discussed in Section 6.

5.2.3. Damping of different vibration modes

Next, we investigate how the damping properties observed for flexural motion carry over to different vibration modes. Knowledge of the vibration damping of individual modes is critical for the design of turbine blades in which complex excitation mechanisms often trigger a broadband multimodal response. Without any loss of generality, analyses are conducted considering the TBC shown in Fig. 3 with a 7YSZ topcoat. Fig. 8 illustrates the main damping peaks characterizing the first four eigenmodes of the beam (Fig. 5). Interestingly, results show a significant increase of the peak temperature associated to higher vibration modes. This phenomenon is consistent with the thermally-activated nature of the relaxation mechanism in which frequency dictates the temperature range of maximum material loss. The maximum damping capacity of each mode, instead, depends on the relaxation strength of the constituent materials and the strain energy density stored in each layer. For instance, Fig. 8 shows that in-plane bending vibrations, mostly dominated by the fourth eigenmode, feature a modest amount of damping at intermediate temperatures compared to the bending or torsional motion of the beam (modes 1–3). The variation of such properties for different design configurations is investigated in the following section.

6. Effects of design parameters on the TBC damping capacity

This section investigates the effects of relevant design parameters on the damping capacity of the first four vibration modes of the TBC. Emphasis is given to the intermediate temperature range

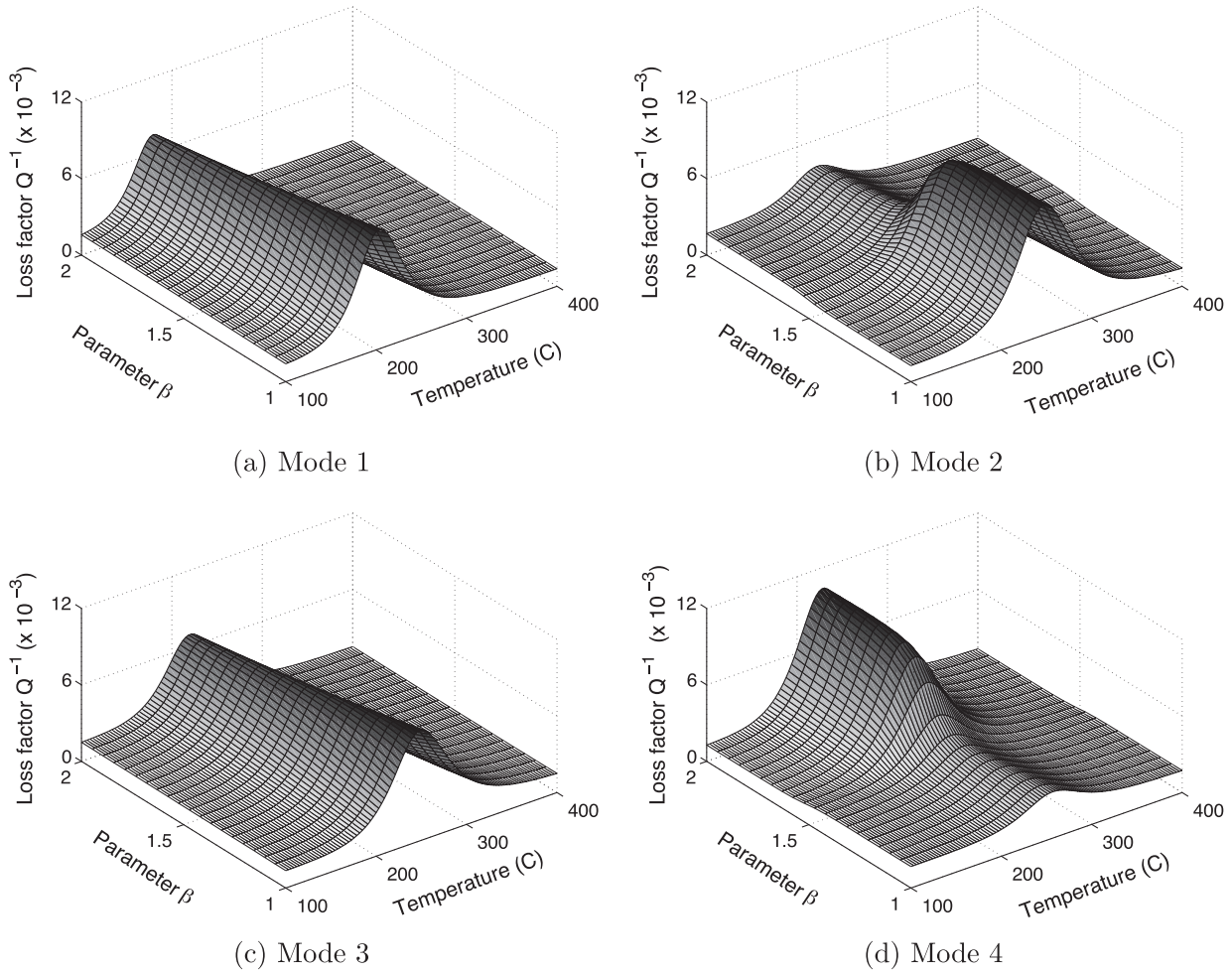


Fig. 11. Vibration damping associated to the first four eigenmodes of the TBC system for different values of the beam length (L), and for $\alpha = 1$.

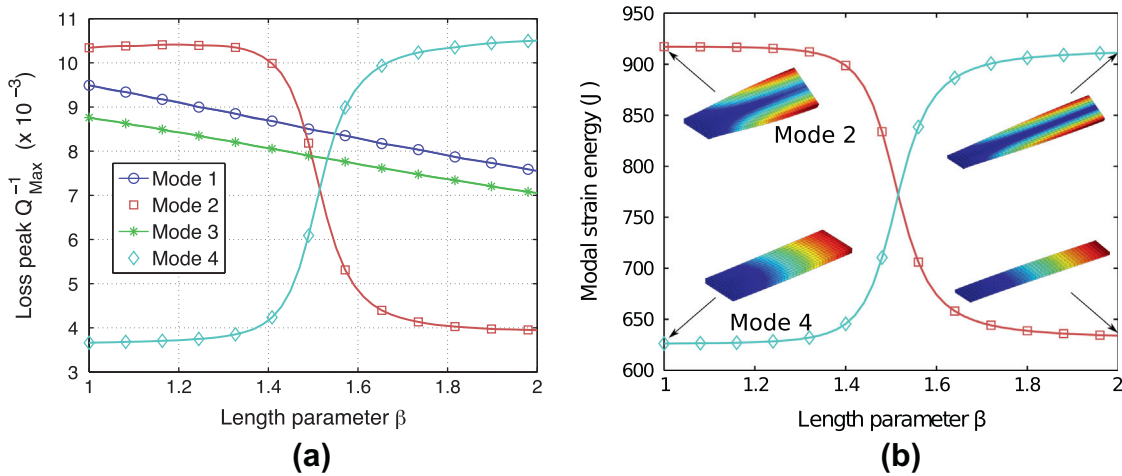


Fig. 12. Variation of the loss peak $Q_{Max}^{-1}(\beta)$ (a), and modal strain energy U_{TOT} (b) of different vibration modes as a function of the length parameter β .

between 100 °C and 400 °C where the main damping peak induced by the oxide layer is observed. The two-layer beam considered in the previous section (Fig. 3) is used as a baseline configuration. Analyses are conducted to separately investigate the effects of the 7YSZ layer thickness (t_{YSZ}) and the beam length (L) on the overall damping performance. Specifically, the thickness of the oxide layer is parametrized as $t_{YSZ} = \alpha t_{PWA}$ where α is a non-dimensional thickness coefficient. Analyses are also conducted for varying beam's

length such that $L = \beta L_0$ in which $L_0 = 16.9$ mm is the length of the baseline configuration, and β is a non-dimensional parameter.

6.1. Effect of the thickness parameter (α)

Fig. 9 illustrates the effect of the 7YSZ layer thickness on the modal loss factor of the TBC. The behavior of the first and second bending modes (Figs. 9a and c) generally corroborates the physical

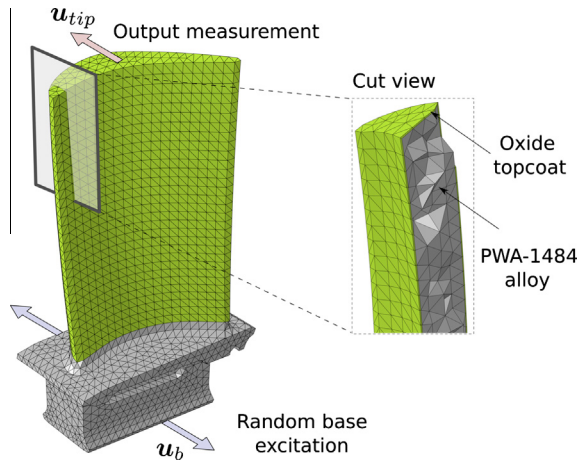


Fig. 13. Finite element discretization of a model coated turbine blade.

intuition underlying the modal strain energy method according to which the damping peak increases as the thickness of the oxide layer is increased. The same results also show a moderate shift of the damping peak towards higher temperatures due to the monotonic increase of the corresponding natural frequencies of vibration.

A rather different behavior characterizes the trend of the first torsional and in-plane bending modes (Figs. 9b and d). For intermediate values of the thickness parameter, in fact, Fig. 9b reveals a counter-intuitive effect whereby the damping peak of the second mode does not increase monotonically with the thickness of the oxide topcoat. Also, Fig. 9d shows a rapid increase of the loss factor associated to the fourth mode occurring at values of $\alpha \approx 1.25$.

These considerations are also illustrated in Fig. 10 which shows the variation of the damping peak $Q_{Max}^{-1}(\alpha) = \max_T Q^{-1}(T, \alpha)$ as a function of the considered thickness parameter α . These results indicate that for $\alpha \lesssim 1.0$ the first three modes feature roughly the same damping capacity which increases monotonically as a function of the topcoat thickness. The loss factor of the second (torsional) mode reaches a maximum at $\alpha \approx 1.15$ after which the damping of the third (in-plane bending) mode becomes more relevant. The existence of stationary points (i.e. maxima and minima) in the functional dependence of damping occurring for specific combinations of the design parameters suggests the possibility of optimizing the performance of the TBC over a broad frequency range.

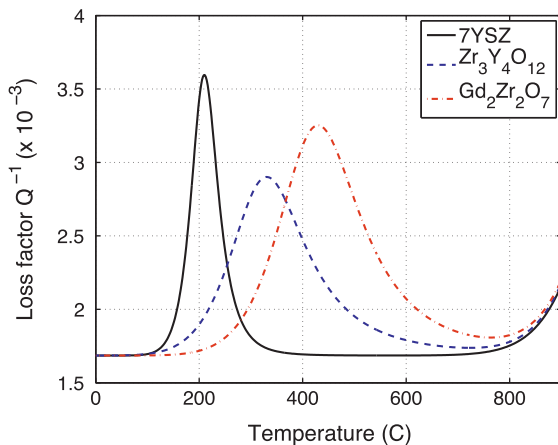


Fig. 14. Comparison between the loss factor variations of the first bending mode of the blade shown in Fig. 13 coated with the oxides shown in Fig. 1.

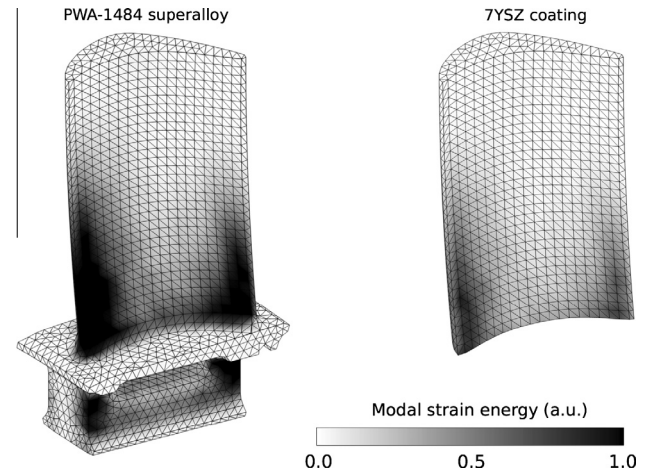


Fig. 15. Distribution of the strain energy (normalized units) associated to the first bending mode of the blade.

Table 2
Modal damping properties of the blade coated with different oxides.

	Mode 1		Mode 2		Mode 3	
	$Q_{max}^{-1} (-)$	$T_p (^\circ\text{C})$	$Q_{max}^{-1} (-)$	$T_p (^\circ\text{C})$	$Q_{max}^{-1} (-)$	$T_p (^\circ\text{C})$
7YSZ	3.60	209.2	3.59	209.2	3.54	209.2
$\text{Y}_4\text{Zr}_3\text{O}_{12}$	2.90	330.1	2.89	330.1	2.84	330.1
$\text{Gd}_2\text{Zr}_2\text{O}_7$	3.25	429.3	3.23	429.3	3.19	429.3

6.2. Effect of the length parameter (β)

The effect of the TBC length on the mechanical loss of the system is investigated by varying the length parameter (β). Results presented in Fig. 11a and c show that the damping of the first and second bending modes monotonically decreases of about 1% as the TBC length is varied from once to twice its original length. As β increases, the results in Fig. 11a and c also indicate that the damping peak of the bending modes tend to occur at lower temperatures due to the lowering of the corresponding natural frequencies. Figs. 11b and d reveal a sudden change of the TBC loss factor associated to the second and fourth modes occurring at a critical value of $\beta_{cr} \approx 1.55$. This behavior is also shown in Fig. 12a showing a direct comparison between the damping peak $Q_{Max}^{-1}(\beta) = \max_T Q^{-1}(T, \beta)$ of the first four modes. Analysis of the mode shapes of the structure, in fact, reveals that the deformation

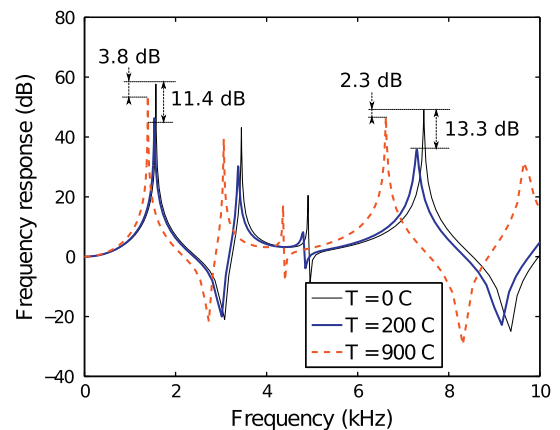


Fig. 16. Frequency response function of the blade coated with a 125 μm thick layer of 7YSZ for increasing temperatures.

patterns of the second and fourth eigenmodes tend to swap as the length parameter is increased above β_{cr} . As shown in Fig. 12b, this corresponds to a redistribution of the strain energy of the two modes which leads to a switch of the corresponding modal damping characteristics.

Although the analysis presented herein focuses on a rather simple geometrical configuration, the obtained results reveal complex or even counter-intuitive trends which must be considered in the design and optimization of oxide layers for multifunctional TBCs.

7. Analysis of a coated turbine blade

In this section, the computational model is used to investigate the damping performance that a TBC can provide to a turbine blade-shaped specimen.

7.1. Finite element model

A prototypical blade, shown in Fig. 13, is discretized using the ABAQUS FEA package while the actual FE computations are conducted using an in-house developed code. The blade, representing a sector of the turbine rotor, is modeled as a PWA 1484 superalloy core that is protected by a 125 μm thick thermal barrier coating. Analyses are conducted using the three oxides previously investigated (i.e. 7YSZ, $\text{Gd}_2\text{Zr}_2\text{O}_7$, and $\text{Y}_4\text{Zr}_3\text{O}_{12}$) whose damping material properties are summarized in Table 1. The Young's modulus and density of the superalloy are reduced by a factor of five to account for the presence of cooling passages and vanes not explicitly incorporated in the model.

The FE mesh of the blade comprises 29,624 4-node linear tetrahedral elements (Fig. 13). The functional dependence of damping on temperature for the three oxides is computed using the modal strain energy method imposing fully-clamped boundary conditions at the base of the blade. The damping properties of the system are also verified through direct frequency response functions obtained by imposing a random excitation to the base of the blade (Fig. 13) as typically done in vibration damping experiments [34]. Also in this case, the maximum discrepancy between the damping estimated with the two methods is below 0.5%.

7.2. Numerical results

A comparison between the damping variations associated with the first bending mode of the coated blade is shown in Fig. 14. The results clearly indicate that the oxide layer generates a significant damping peak at intermediate temperatures, ranging from 200 °C to 400 °C depending on the relaxation parameters of the specific oxide being considered, and reproduce the temperature dependence measured in the flexural beam. Fig. 14 however shows that the magnitude of the damping peak is significantly lower than what observed for the cantilever beam case. This can be understood directly from the modal strain energy method since the relative volume of the coat and superalloy is reduced on the blade. Fig. 15 shows that, contrary to many samples used for simple tests [14,15,35,36], the region of high strain energy density, and hence, damping are mostly localized in the blade.

A summary of the damping performance associated with the first three vibration modes for different oxides are reported in Table 2. Interestingly, the numerical results indicate that the maximum loss factor Q_{max}^{-1} and the peak temperature T_p are almost insensitive to the specific mode of vibration of the blade. Although Table 2 only shows data associated with the first three modes, we observe similar trends also for higher order vibration mechanisms (not shown for clarity), thus providing robust damping characteristics over a broad range of frequencies.

The direct frequency response of the system is also computed to illustrate the effect of damping on the blade's steady-state response at various temperatures. Analysis are presented for a blade coated with a 7YSZ oxide layer, but analogous results are also observed for the other oxides considered in this study. Fig. 16 illustrates the frequency response function between the imposed base motion \mathbf{u}_b and the blade's tip displacement \mathbf{u}_{tip} (see Fig. 13). The response function computed at $T = 0$ °C is used as a reference to estimate the attenuation provided to the system by the point defect relaxation mechanism in the oxide layer. Remarkably, the results indicate that at the peak temperature of about 200 °C, the TBC reduces by about 12 dB the amplitude of all the resonance modes up to 10 kHz.

8. Conclusions

A finite element approach is used to predict the vibrational damping in a multi-layer TBC system due to point defect relaxation induced by the oxide topcoat. The proposed framework is based on a description of damping as the result of anelastic relaxation due to point defect rearrangement in highly defective oxides. The functional dependence of mechanical loss on temperature and vibration frequency is conveniently implemented in a FE framework which allows estimation of the damping properties of complex three-dimensional shaped TBCs. Numerical analyses are conducted using both the direct frequency response method and, more conveniently, the modal strain energy method which is found to provide nearly identical results at a fraction of the computational cost.

Comparison with experimental data shows that the proposed framework correctly captures the damping variation of a multi-layer system based on experimentally-informed material properties derived for each of the constituent materials. The approach is also used to estimate how the damping properties, typically obtained for flexural motion only, carry over to other vibration modes. Finally, parametric analyses illustrate how the proposed approach can estimate the effects of several design parameters on the damping performance of a TBC system. The obtained results highlight a complex functional dependence of damping on the geometrical parameters of the system, which must be considered for the design of oxide layers for multifunctional TBCs.

Acknowledgements

The authors would like to acknowledge support of this work through an AF-SBIR Grant from DVTI.

References

- [1] B.L. Koff, B.L. Koff, *Journal of Propulsion and Power* 20 (4) (2004) 577–595.
- [2] J.H. Griffin, *International Journal of Turbo and Jet Engines* 7 (3–4) (1990) 297–308.
- [3] C. Yu, J. Wang, Q. Li, *Journal of Vibration and Control* 17 (8) (2011) 1149–1157.
- [4] A. Evans, D. Clarke, C. Levi, *Journal of the European Ceramic Society* 28 (7) (2008) 1405–1419.
- [5] D. Clarke, C. Levi, *Annual Review of Materials Research* 33 (1) (2003) 383–417.
- [6] R.V. Hillery, et al., *Coatings for High-Temperature Structural Materials: Trends and Opportunities*, National Materials Advisory Board Report, National Academy Press, Washington, DC.
- [7] U. Schulz, C. Leyens, K. Fritscher, M. Peters, B. Saruhan-Brings, O. Lavigne, J. Dorvaux, M. Poulain, R. Mévrel, M. Caliez, *Aerospace Science and Technology* 7 (1) (2003) 73–80.
- [8] K. Cross, W. Lull, R. Newman, A.R. Cavanagh, *Journal of Aircraft* 10 (11) (1973) 689–691.
- [9] C. Chia, K. Khor, Y. Gu, F. Boey, *Thin Solid Films* 405 (1) (2002) 146–152.
- [10] F. Soechting, *Journal of Thermal Spray Technology* 8 (4) (1999) 505–511.
- [11] L. Yu, Y. Ma, C. Zhou, H. Xu, *International Journal of Solids and Structures* 42 (11) (2005) 3045–3058.
- [12] D.R. Clarke, S.R. Phillpot, *Materials Today* 8 (6) (2005) 22–29.

- [13] R.C. Reed, *The Superalloys: Fundamentals and Applications*, Cambridge University Press, 2006.
- [14] G. Gregori, L. Li, J. Nychka, D. Clarke, *Materials Science and Engineering: A* 466 (1) (2007) 256–264.
- [15] A. Limarga, T. Duong, G. Gregori, D. Clarke, *Surface and Coatings Technology* 202 (4) (2007) 693–697.
- [16] M. Weller, R. Herzog, M. Kilo, G. Borchardt, S. Weber, S. Scherrer, *Solid State Ionics* 175 (1) (2004) 409–413.
- [17] W. Hemmann, T.V. Ort, H. Sockel, *Journal de Physique IV* 6 (8) (1996) 223–226.
- [18] J. Wachtman Jr, L. Doyle, *Physical Review* 135 (1A) (1964) A276.
- [19] A. Nowick, *Advances in Physics* 16 (61) (1967) 1–47.
- [20] R. Lakes, J. Quackenbush, *Philosophical Magazine Letters* 74 (4) (1996) 227–232.
- [21] B. Berry, *Acta Metallurgica* 10 (4) (1962) 271–280.
- [22] A.S. Nowick, B.S. Berry, *Anelastic Relaxation in Crystalline Solids*, vol. 1, Academic Press, 1972.
- [23] J. Wachtman Jr, *Physical Review* 131 (2) (1963) 517.
- [24] A. Nowick, W. Heller, *Advances in Physics* 14 (54) (1965) 101–166.
- [25] M. Callens-Raadschelders, R. De Batist, R. Gevers, *Journal of Materials Science* 12 (2) (1977) 251–263.
- [26] R. Carnahan, J. Brittain, *Journal of Applied Physics* 34 (10) (1963) 3095–3104.
- [27] D.R. Bland, *The Theory of Linear Viscoelasticity*, vol. 10, Pergamon Press, New York, 1960.
- [28] R. Christensen, *Theory of Viscoelasticity: An Introduction*, Academic press, 1982.
- [29] A. Shani, A. Milani, N. Vermaak, K. Bertoldi, T. Scarinci, M. Gerendas, *Journal of Applied Mechanics* 79 (2012) 061019.
- [30] C.D. Johnson, D.A. Kienholz, *AIAA Journal* 20 (9) (1982) 1284–1290.
- [31] T. Hughes, *The Finite Element Method: Linear Static and Dynamic Finite Element Analysis*, Dover, Publications, 2000.
- [32] K. McConnell, P. Varoto, *Vibration Testing: Theory and Practice*, John Wiley & Sons, 1995.
- [33] M. Weller, H. Clemens, G. Haneczok, *Materials Science and Engineering: A* 442 (1) (2006) 138–141.
- [34] D. Zhu, R.A. Miller, K.P. Duffy, L.J. Ghosn, High temperature damping behavior of plasma-sprayed thermal barrier and protective coatings, in: 33rd International Conference and Exposition on Advanced Ceramics and Composites, American Ceramic Society, 2009.
- [35] N. Tassini, K. Lambrinou, I. Mircea, S. Patsias, O. Van der Biest, R. Stanway, Comparison of the damping and stiffness properties of 8 wt% yttria stabilized zirconia ceramic coating deposited by the APS and EB-PVD techniques, in: Smart Structures and Materials, International Society for Optics and Photonics, 2005, pp. 109–117.
- [36] N. Tassini, K. Lambrinou, I. Mircea, M. Bartsch, S. Patsias, O. Van der Biest, *Journal of the European Ceramic Society* 27 (2) (2007) 1487–1491.